OPTICA

Scalable photonic integrated circuits for high-fidelity light control

Adrian J. Menssen,[1,†,*] Artur Hermans,[1,†] Ian Christen,[1] Thomas Propson,[1] Chao Li,[1] Andrew J. Leenheer,[2] Matthew Zimmermann,[3] Mark Dong,[1,3] Hugo Larocque,[1] Hamza Raniwala,[1] Gerald Gilbert,[4] Matt Eichenfield,[2,5] and Dirk R. Englund[1]

[1]Massachusetts Institute of Technology, Cambridge, Massachusetts 02139, USA
[2]Sandia National Laboratories, Albuquerque, New Mexico 87185, USA
[3]The MITRE Corporation, Bedford, Massachusetts 01730, USA
[4]The MITRE Corporation, Princeton, New Jersey 08540, USA
[5]University of Arizona, Tucson, Arizona 85721, USA
[†]These authors contributed equally to this work.
*amenssen@mit.edu

Received 9 March 2023; revised 31 August 2023; accepted 3 September 2023; published 13 October 2023

Advances in laser technology have driven discoveries in atomic, molecular, and optical (AMO) physics and emerging applications, from quantum computers with cold atoms or ions, to quantum networks with solid-state color centers. This progress is motivating the development of a new generation of optical control systems that can manipulate the light field with high fidelity at wavelengths relevant for AMO applications. These systems are characterized by criteria: (C1) operation at a design wavelength of choice in the visible (VIS) or near-infrared (IR) spectrum, (C2) a scalable platform that can support large channel counts, (C3) high-intensity modulation extinction and (C4) repeatability compatible with low gate errors, and (C5) fast switching times. Here, we provide a pathway to address these challenges by introducing an atom control architecture based on VIS-IR photonic integrated circuit (PIC) technology. Based on a complementary metal–oxide–semiconductor fabrication process, this atom-control PIC (APIC) technology can meet system requirements (C1)–(C5). As a proof of concept, we demonstrate a 16-channel silicon-nitride-based APIC with (5.8 ± 0.4) ns response times and >30 dB extinction ratio at a wavelength of 780 nm.

https://doi.org/10.1364/OPTICA.489504

1. INTRODUCTION

Quantum technologies have reached a pivotal stage where the number of qubits is approaching the limit of classical simulability [1,2]. A key challenge in achieving practically useful quantum technology lies in the scalable, coherent control of the individual qubits. As potential candidates for qubits, several platforms that rely on atomic or atom-like systems have emerged, including cold atoms [3,4], ions [5–7], and atom-like emitters in solids [8,9]. Many suitable optical transitions of these systems lie in the visible to near-infrared wavelength range. Previous work towards quantum control has relied on using a limited number of local addressing beams modulated by bulk acousto-optic devices [3,5,10,11]. This approach becomes problematic when scaling beyond tens of optical control channels. Here, we address this bottleneck by introducing photonic integrated circuit (PIC) technology based on compact, resonant, and high-extinction modulators and fabricated in a process compatible with modern complementary metal–oxide–semiconductor (CMOS) manufacturing.

The development of on-chip high-speed modulators has mainly been driven by telecom applications [12]. However, O- and C-band platforms (e.g., silicon [13] and indium phosphide [14]) are incompatible with visible-wavelength operation. Silicon nitride (SiN) is a leading photonic integration platform compatible with visible-wavelength operation [15]. SiN is transparent down to blue wavelengths [16] and extremely low waveguide propagation losses have been demonstrated (<0.1 dB/m at 1.6 μm [17] and 22 dB/m at 450 nm [16]). Moreover, SiN photonic integrated circuits are manufacturable in CMOS fabrication processes and have been demonstrated to enable high-power handling, with watt-level waveguide-coupled optical powers reported at 1.6 μm [18]. While SiN's thermo-optic effect allows slow modulation with ∼μs response times [19], this limit in modulation rate is problematic for fast optical quantum control. Recently, SiN platforms with aluminum nitride (AlN) piezoelectric actuators have been introduced, enabling visible and near-infrared light modulation with ∼ns response times [20–22].

In this work, we present an atom-control photonic integrated circuit (APIC) platform intended for high-fidelity local quantum control of atomic and atom-like systems, notably with high extinction (C3) and repeatability (C4). The platform relies on SiN photonic integrated circuits with fast AlN piezoelectric actuators [20], thereby satisfying criteria (C1) and (C5). Our APICs are

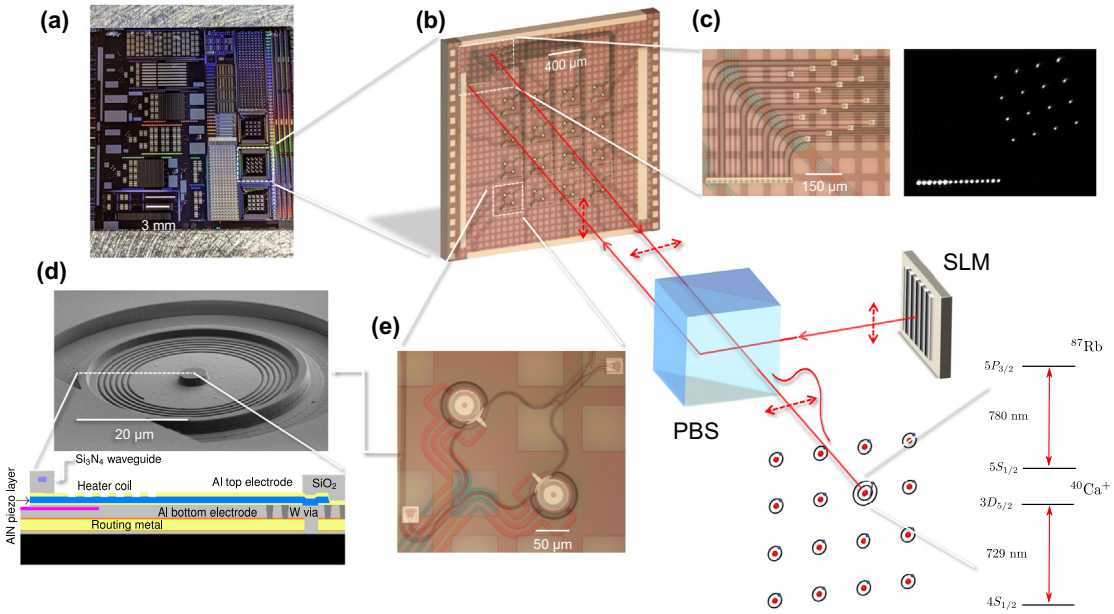

Fig. 1. Atom-control photonic integrated circuit (APIC) platform. (a) Photograph of full reticle. (b) APIC modulator array with a modulator pitch of 420 µm. (c) 4 × 4 out-coupling and 1 × 16 in-coupling area. Chip detail (left) and camera image with light coupled into all ports (right). (d) SEM image of individual ring (top). Schematic cross section of device with piezo-stack and waveguiding layers illustrated. (e) DRMZM with local in- and out-coupling gratings, which can be used as an alternative to the grating couplers in (c). Bottom right: illustration of setup. An SLM projects light onto the APIC, where the light is modulated and after passing through a PBS imaged onto an array of (artificial) atoms. The input light path onto the SLM is not shown.

fabricated at temperatures < 500°C in a 200 mm wafer, CMOS-compatible process, permitting co-integration with electrical circuits for driving control voltages and implementing feedback [23]. See Appendix A for more details on fabrication and packaging. This approach enables large channel counts, thereby fulfilling criterion (C2).

The illustration in Fig. 1 shows our proof-of-concept APIC with an array of 16 high-speed dual-ring-assisted Mach–Zehnder modulators (DRMZMs) [24] arranged in a 4 × 4 grid. We show that these DRMZMs can, in a fabrication-tolerant way, achieve voltage-programmable light extinction in a compact footprint, as required for high-fidelity quantum control devices with large channel counts. We demonstrate that the spread in ring resonant frequencies due to fabrication non-uniformity, a major issue in large-scale PICs [25], can be eliminated using integrated thermo-optic heaters for tuning. Moreover, power dissipation from such tuning can be avoided by permanently shifting the resonances via laser-based trimming.

2. RESULTS

Interfacing between the laser source and the APIC is a large programmable switch to uniformly distribute light into each DRMZM (Fig. 1): in this case, implemented holographically via a commercial megapixel liquid crystal spatial light modulator (SLM) [26]. While such SLMs—with ∼100 Hz update rate—cannot satisfy the speed criterion (C5) directly, they are ideal for static optical power fanout to balance light across the high-speed DRMZMs in a scalable and reconfigurable way. By delegating the input light control to the millions of stable degrees of freedom on the SLM, we save the need for large-footprint, carefully balanced, fabrication-sensitive splitter trees [27]. With its single input, a splitter tree is also more prone to catastrophic failure.

Vertically radiating gratings couple the holographically distributed light into and out of each DRMZM. We route the inputs and outputs of the modulators together in one corner of the APIC [Fig. 1(c)], where we use a 1 × 16 array of grating couplers for coupling in, and a two-dimensional 4 × 4 array of grating couplers for coupling the modulated light out towards the target atomic systems. Notably, the input and output grating couplers are oriented at 90° with respect to each other, such that a polarizing beam-splitter (PBS) can be used to separate the in- and outgoing light. At the system level, a relevant characteristic is the optical power efficiency of each device $\eta = \max_V(|A_{\text{out}}(V)|^2)/|A_{\text{in}}|^2$, where $A_{\text{in,out}}$ is the field amplitude at the input and output of a DRMZM, and V is applied voltage [Fig. 2(a)]. Inefficiency is dominated by losses in the grating couplers. To boost efficiency, we take advantage of the aluminum layer underneath the grating, which serves as the top piezo-electrode shown in Fig. 1(d). The reflective aluminum directs light upward and greatly enhances coupling efficiency [28]. The measured SLM transmission is −2.2 dB (diffraction efficiency into fanout beams). The DRMZM transmission including gratings is −11.5 dB. The total transmission is therefore −14 dB.

The large channel count criterion (C2) motivates high optical channel density ρ. The resonant phase modulators used in the DRMZM afford a higher degree of compactness compared with conventional phase modulators. With an inter-device spacing of 420 µm in our demonstrator, cf. Fig. 1(b), we achieve a device density of approximately six devices per square-millimeter $\rho \sim 6/\text{mm}^2$. If we use the entire reticle (2.2 cm × 2.2 cm) for our array, ∼2900 devices can be realized, with further improvements to compactness possible.

A. Performance Metrics for Quantum Gates

We now establish key performance metrics of our device. These metrics are guided by the application requirements for optical

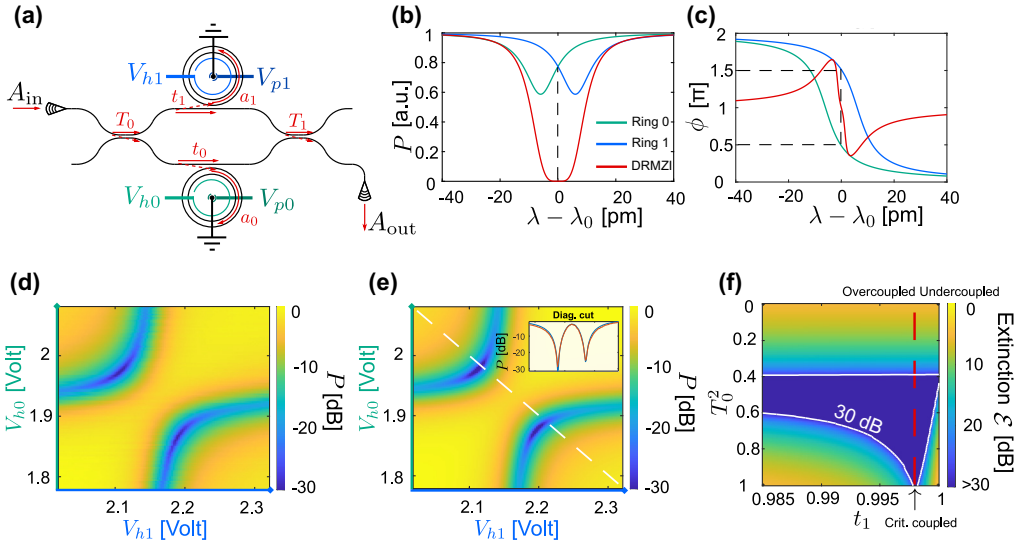

Fig. 2. Dual-ring-assisted Mach–Zehnder modulator (DRMZM). (a) Schematic of a DRMZM. Input light amplitude is indicated as A_{in}, along with the transmissive amplitude coupling coefficients for beamsplitters ($T_{0,1}$) and ring-waveguide ($t_{0,1}$), and the piezo- $V_{p0,1}$ and heater voltages $V_{h0,1}$ used for modulation and long-range tuning. $a_{0,1}$ represents the single round trip ring transmission. (b) Transmitted powers $P = |A_{\text{out}}|^2$ around a target wavelength λ_0 for individual rings and the DRMZM. (c) Phase $\phi = \arg(A_{\text{out}})$ responses. Plots (b) and (c) assume identical rings and beamsplitters. (d) Measured normalized power $P = 10\log_{10}(|A_{\text{out}}|^2/\max(|A_{\text{out}}|^2))$ dB as a function of heater voltages. (e) Fit of (d) to our model with the parameters: $a_0 = 0.9962 \pm 1.7 \cdot 10^{-4}$, $a_1 = 0.9975 \pm 1.9 \cdot 10^{-4}$, $t_0 = 0.983 \pm 1.8 \cdot 10^{-4}$, $t_1 = 0.9816 \pm 2 \cdot 10^{-4}$. $T_{0,1}^2 = 0.5$ is fixed. The R^2 value of the fit is 0.96. These values for $a_{0,1}$ yield fitted intrinsic quality factors $Q_{i0} = 2.7 \cdot 10^5 \pm 1.34 \cdot 10^4$ and $Q_{i1} = 4 \cdot 10^5 \pm 3 \cdot 10^4$. The inset shows the profile along dotted diagonal line (red data, blue fit). (f) Numerically extracted extinction achievable as a function of T_0^2 ($T_1^2 = 0.5$) and t_1 ($t_0 = 0.985$). We set $a_0 = a_1 = 0.998$. Blue region inside the contour indicates better than 30 dB extinction.

quantum control. The Rabi frequency of an optically driven atomic transition depends on the electrical field $\vec{E}(x, y, t)$ (transverse coordinates x, y) at the position of the atom. Experimentally, we measure the optical power using a photodiode $P(t) = \int I(x, y, t)\mathrm{d}A$, where $I(x, y, t) \propto |\vec{E}(x, y, t)|^2$. For simplicity, we consider a rectangular π control pulse with constant light intensity I_1 in the "on" state. The extinction is $\mathcal{E} = \frac{I_0}{I_1}$, where I_0 is the residual light intensity in the "off" state. We define the intensity normalized pulse error by $\Delta\mathcal{I} = \frac{\Delta I_1}{I_1}$. Given an intensity error ΔI_1, the "on" state error $1 - \mathcal{F}_1 \sim (\Delta\mathcal{I})^2$ is proportional to the square of the intensity error. The "off" state error $1 - \mathcal{F}_0 \sim \mathcal{E}$ scales linearly with extinction (see Supplement 1, Section 1 and [29]). $\mathcal{F}_i$ is the fidelity in state i (1=on, 0=off) (see Supplement 1, Section 1 for a definition). The requirements on $\mathcal{E}$ and $\Delta\mathcal{I}$ for low pulse error correspond to criteria (C3) and (C4). Criterion (C5) for fast switching times $\delta\tau$ follows from the need for many gate operations to be executed during the lifetime of the quantum state [6,30,31]. Typical gate durations are in the range of tens to hundreds of nanoseconds for single-qubit rotations or entangling gates for cold atom systems [31,32], atom-like emitters in solids [33], and in the range of microseconds to milliseconds for trapped ion motional gates [6,7].

B. Modulator Architecture

The DRMZM, schematically shown in Fig. 2(a), lies at the core of our architecture. It consists of a Mach–Zehnder interferometer (MZI), with two 50:50 beamsplitters, and a ring resonator coupled to each arm of the interferometer.

Each ring resonator acts as a coupled phase and amplitude modulator with a well-known response function [34]:

$$A_{\text{SRout}} = A_{\text{SRin}} e^{i(\pi+\varphi)} \frac{a - te^{-i\varphi}}{1 - tae^{i\varphi}}, \tag{1}$$

where $a_{\text{SRin,out}}$ is the field amplitude at the input and output of a single ring, a is the attenuation coefficient for a single round trip in the ring, t is the bus waveguide's self-coupling coefficient, and φ is the round trip phase. For fast modulation, we rely on piezoelectric actuation, cf. Fig. 4(e). In the overcoupled regime ($t < a$), the ring acts as a "force-multiplier" for phase, where the small phase shifts possible through the fast but weak piezoelectric actuators can be amplified to a $\sim 2\pi$ phase shift per ring [Fig. 2(c)] [35]. Each ring is additionally equipped with a local heater [Fig. 1(d)] for long-range tuning to compensate for fabrication variations (as discussed in the next section). Each overcoupled ring also modulates the amplitude in each arm of the MZI. By choosing the operating point of both rings correctly, we can select amplitude and phase in each arm to achieve in principle perfect destructive interference at the output port of the second beamsplitter. Furthermore, the two available degrees of freedom (phase tuning in both rings) afford full amplitude and phase control over the output electrical field (see Supplement 1, Section 2). This full field control is especially desirable in protocols where the phase of the optical field needs to be changed quickly [36].

The simulated phase and amplitude response for both the isolated rings and the DRMZM is shown in Figs. 2(b) and 2(c) as a function of wavelength, assuming the ideal situation where the beamsplitters and rings are identical. We achieve perfect extinction at the output port when the differential phase is π and the light amplitude in both MZI arms are exactly balanced to match the amplitude splitting ratio of the out-coupling beamsplitter. Figure 2(d) shows the experimentally measured output light power as a function of the heater voltages for each ring, which are used for

long-range tuning to this ideal operating point. The points of minimum power are clearly visible in both branches of the "avoided crossing" of the two resonances ($\mathcal{E} = 31$ dB in the top branch and 30 dB in the bottom branch).

We fit the experimental data to a model with parameters defined in Fig. 2(a). The result is shown in Fig. 2(e), in good agreement with the measured data ($R^2 = 0.96$).

DRMZM extinction—a critical figure of merit for (C3)—is robust to large fabrication variations, in contrast to regular MZMs. In MZMs, the principal limitation to the achievable light extinction is given by how well the two beamsplitters comprising the MZM are matched to each other. Unequal beamsplitter ratios in the DRMZM are manifest in the output power distribution [Fig. 2(e)] as a breaking of mirror symmetry along the diagonal. The two points of minimum power translate along both branches as the difference between the beamsplitters increases. In Fig. 2(f), we show that a high extinction ratio is achievable for a wide range of fabricated parameters. In our case, we attribute the primary limitations to the measured extinction ratio to originate from small drifts of the resonance position during the measurement along with input polarization misalignment.

C. Resonance Tuning

Fabrication-induced variations in resonance frequency are a major issue in integrated photonic devices [25]. While our piezoelectric actuators are fast, their range is not sufficient to account for this fabrication-induced resonance spread. In our system, as-fabricated resonances are distributed over hundreds of picometers or tens of linewidths, making modulation of a single laser frequency across the full array of devices impossible. To retune the system to a common resonance, we developed a combination of tunable and nonvolatile resonance shifting based on (i) integrated heaters [37] and (ii) laser trimming [38–40]. Figure 3 plots the resonance positions for 10 different DRMZMs before and after alignment.

For reconfigurable thermo-optic tuning, heating power is generated by a resistive coil in proximity of the waveguide, as shown in Fig. 1(d). We measure resonance tuning efficiencies of

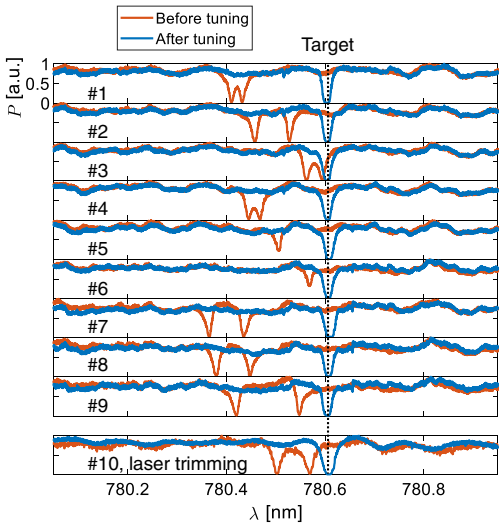

Fig. 3. Resonance tuning of DRMZMs. The top nine panels show the simultaneous alignment of the 18 resonances of nine channels to a target wavelength (780.6 nm) using the integrated heaters. The bottom panel shows resonance alignment for a 10th channel using nonvolatile laser trimming.

Table 1. Performance Metrics

Metric	Symbol	Value	Criterion
Wavelength	λ_0	780 nm	C1
Channel density	ρ	$6/\text{mm}^2$	C2
Power efficiency	η	7%	C2
Extinction	$\mathcal{E}$	>30 dB	C3
Infidelity "off" state	$1-\mathcal{F}_0$	$1.5\cdot10^{-3}$	C3
Pulse error	$\Delta\mathcal{I}$	$1\cdot10^{-3}$	C4
Infidelity "on" state	$1-\mathcal{F}_1$	$0.6\cdot10^{-6}$	C4
10%–90% rise time	$\delta\tau$	(5.8 ± 0.4)ns	C5

6 pm/mW (see Supplement 1, Section 4). Negating fabrication spread requires powers of the order of 50 mW per ring. This may prove a hindrance as we scale to 1000s of channels. We therefore developed a nonvolatile laser trimming process.

To complement thermal tuning and relax requirements on dissipated power, we can permanently but non-reversibly shift resonances by trimming rings with a blue laser, notably without degradation of the optical quality factor (see Supplement 1, Section 5). The accessible trimming range is larger than the observed variations in resonance positions, and operates with sufficient precision to target within the limited range of piezoelectric actuation.

To limit the need for post-fabrication tuning, future devices may include adiabatic rings, which have been demonstrated to be more robust against fabrication variations [19].

D. Fast Switching

With resonances aligned at a desired operating point, we next demonstrate that our DRMZMs operate as fast light modulators with repeatable switching at high extinction ratios under piezoelectric actuation (C3–C5). To enhance resonance stability, we strongly overcouple the rings (effectively broadening the linewidth), while ensuring that each ring can be actuated to $\sim\pi/2$ phase over the voltage range of 30 V achieved by our amplifiers. Our measured actuation efficiency conforms with the previously demonstrated 0.4 pm V^{-1} [20]. The driving voltage of our devices can be reduced by using enhanced piezo-materials such as scandium-doped AlN, which has a piezoelectric response that is up to five times larger than that of AlN [41]. We can also choose to operate at lower driving voltages at the expense of a reduced light efficiency, as lower driving voltages result in smaller resonance shifts. Figure 4(a) plots the measured normalized individual pulse area for a 1 MHz rectangular pulse train of 1 ms total duration. We chose these pulse train properties with Rydberg–Rydberg interaction mediated gates in mind, as typical Rydberg lifetimes are $\sim$100 µs to <1 ms, at typical ground-state-Rydberg Rabi frequencies of 1−10 MHz [32]. This measurement indicates a pulse area consistency with a (1σ) standard deviation of $\Delta\mathcal{I} = 9.8\cdot10^{-4}$ (C4). Figure 4(d) shows the fast switching behavior of our device (C5). We observe a 10%–90% rise time of (5.8 ± 0.4) ns. Further, we demonstrate a high extinction ratio of $\mathcal{E}\sim30$ dB during switching (C3). Figure 4(b) shows the extinction ratios for a pulse sequence with randomized pulse lengths (between 300 ns and 1 µs), as displayed in Fig. 4(c) (see Supplement 1, Section 3 for eye diagrams and a measurement of the modulation bandwidth). Table 1 summarizes key performance metrics.

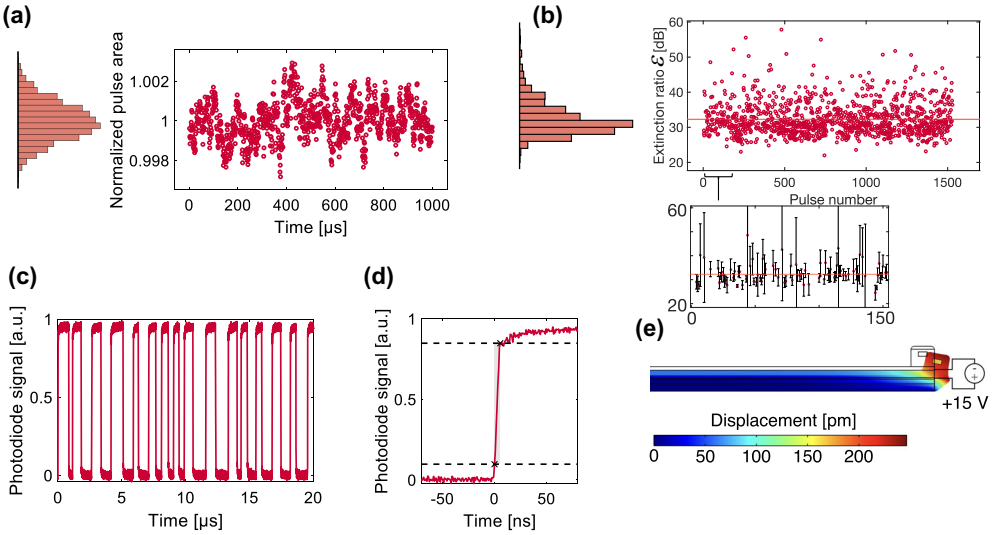

Fig. 4. Fast switching using piezoelectric actuators. (a) Normalized pulse area versus time. Each point corresponds to a single pulse. Pulse area consistency (1σ) $\Delta\mathcal{I} = 9.8 \cdot 10^{-4}$ for a pulse train of 1 ms duration. These data use duty cycle 50% and frequency 1 MHz. (b) Extinction ratio $\mathcal{E}$ for a random pulse train with pulse durations in between 300 ns and 1000 ns. Inset with error bars. Mean extinction is 32.3 ± 0.14 dB, indicated by horizontal red line. (c) Randomized pulse sequence. The optical output power in the "on" state is 0.2 mW. (d) Determination of the 10%–90% rise time $\delta\tau$. Black dashed lines indicate the 90% and 10% levels. (e) Simulated ring waveguide displacement resulting from applied voltage of 15 V to the bottom electrode of the piezo-stack.

3. DISCUSSION

We introduced a SiN atom-control photonic integrated circuit (APIC) technology intended for scalable quantum control of atomic systems. Fabricated in a 200 mm wafer, CMOS-compatible process, our APICs achieve pulse errors of $9.8 \cdot 10^{-4}$, extinction ratios >30 dB, and rise times of (5.8 ± 0.4)ns, enabling high-precision optical manipulation of quantum states. Furthermore, we showed that the fabrication-induced variations in resonance frequencies can be compensated for by integrated heaters or non-volatile laser trimming, an essential feature for large-scale resonant PICs. The CMOS compatibility of our fabrication process also enables us to manufacture our photonics architecture directly on top of a high-voltage CMOS driver [42]. There are no fundamental limits to scaling our approach to thousands of channels in such an architecture. While we demonstrated operation at around 780 nm, the design of our devices can be tuned to allow operation at any wavelength within SiN's transparency window. Replacing SiN with wide-bandgap waveguiding materials such as aluminum oxide [43] or nitride [8] could enable operation down to UV wavelengths.

We anticipate that coherent optical control by our APIC platform will find widespread application for manipulating quantum systems, especially for atomic quantum control on arrays of neutral atoms [3,4,9,44], ions [6,7], and color centers [8,9]. In our future work, we plan to use a second SLM to reconfigure the modulated beams coming out of our chip such that they match with the configuration of the targeted quantum system, whether this is an array of atoms or color centers residing in a cryostat. This approach has been introduced in [26]. Our modulator architecture could also be directly combined on-chip together with ion traps or heterogeneously integrated with diamond color center waveguides [8]. In simulated condensed matter systems [45], we anticipate that our architecture will enable experimental studies beyond global many-body effects and towards local phenomena such as topological defects and their associated quasi-particles [46].

APPENDIX A

1. Device Fabrication

Our devices are fabricated at Sandia National Laboratories on 200 mm silicon wafers using deep ultraviolet optical lithography [20]. The devices have three metal layers interconnected through vias: a routing layer (Al/Ti), a bottom electrode layer (Al), and a top electrode layer (Al). A piezoelectric AlN layer sandwiched in between the bottom and top electrode layers enables piezoelectric actuators. The bottom and top electrode layers are connected to bond pads through vias and the bottom metal routing layer. On top of the piezoelectric actuators, a SiN waveguide layer (300 nm thickness) is fabricated with silicon dioxide cladding above and below. An amorphous silicon release layer fabricated below the piezoelectric actuators can be used to undercut devices via XeF_2 etching [20]. The devices presented in this work are not released, to allow for a larger modulation bandwidth due to the "stiffer" resulting actuator. In Fig. 5, the on-chip electrical routing is illustrated.

2. Packaging and Drivers

After fabrication, we dice the wafers into chips. The chips are glued on a copper block using a thermal epoxy. Wire bonds connect the chip to a printed circuit board (PCB). Figure 6 shows a picture of the wire bonded chip. The PCB connects our chip to the heater and piezoelectric actuator drivers. The heaters are driven by Qontrol Q8iv modules delivering a maximum voltage of 12 V and a maximum current of 24 mA (per channel). The piezoelectric actuators are driven by Spectrum M2p.6566-x4 arbitrary waveform generators with a maximum output rate of 125 MS/s and an output level of ± 3 V into 50Ω. This signal is amplified by a factor of five to ± 15 V using high-bandwidth electronic amplifiers (Texas Instruments THS3491) on the PCB, fed by a ± 16 V power supply. The maximum slew rate of the amplifiers is 8000 $V\mu s^{-1}$. We also

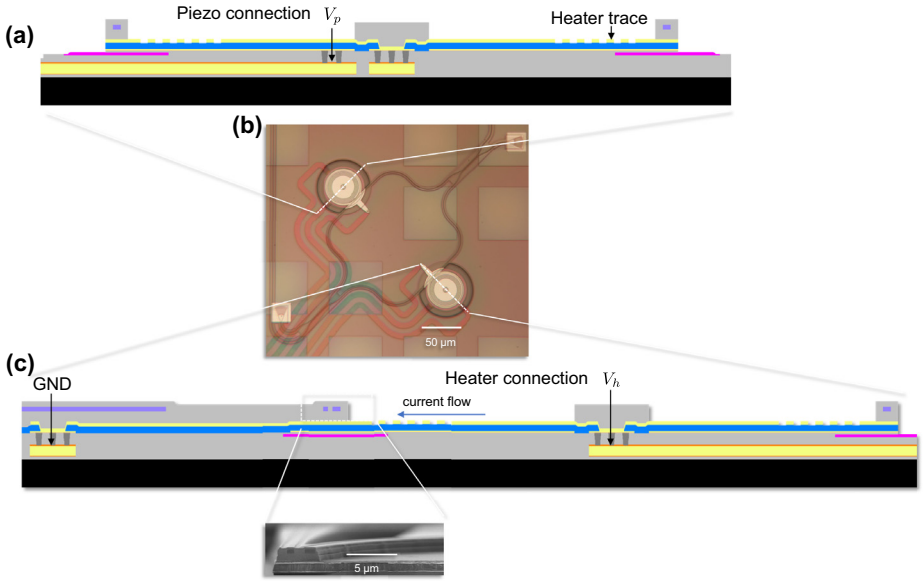

Fig. 5. We show two orthogonal cross sections through the wafer. (a) Cut showing the connection to the bottom electrode of the piezo-actuator. Close to the waveguide, we can see the cross section of the heater spiral in the top metal. (b) Microscope image illustrating the position for the cuts in (a) and (c). (c) Cut showing the ground (GND) and heater connections. The heating current flow from the heater terminal to ground via the high-resistance heater spiral is shown. An SEM inset shows the region around the coupling waveguide.

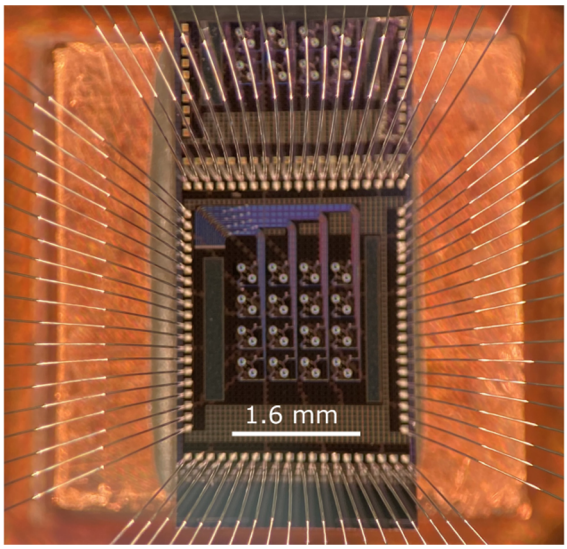

Fig. 6. Wire bonded chip on top of copper block. We can see the individual devices arranged in a 4×4 grid at the center of the chip. Image credit: Merrimack Micro.

note that multiples of our modulator chips could be combined in a single package to achieve a larger number of channels. Several SLMs or a single higher-resolution SLM may be used for fanout.

Funding. U.S. Department of Defense (NDSEG Fellowship); Massachusetts Institute of Technology (Jacobs Presidential Fellowship); National Science Foundation (DMR-1747426, Graduate Research Fellowship Program); Belgian American Educational Foundation (Fellowship); U.S. Department of Energy (Quantum Systems Accelerator (QSA)); Defense Advanced Research Projects Agency (ONISQ); MITRE Corporation (Moonshot program); Alexander von Humboldt-Stiftung (Feodor Lynen Research Fellowship).

Acknowledgment. The authors acknowledge Christoper Panuski and Sivan Trajtenberg-Mills for contributions to the slmsuite software package https://github.com/QPG-MIT/slmsuite, along with Lilia Chan for designing the chassis and chip mount, and Kevin Dauphinais for designing the PCB of the electronic driver. We thank Yin Min Goh for helping with data collection during the review process.

Disclosures. DRE: QuEra Computing (I,P,S).

Data availability. Data underlying the results presented in this paper are not publicly available at this time but may be obtained from the authors upon reasonable request.

Supplemental document. See Supplement 1 for supporting content.

REFERENCES

1. F. Arute, K. Arya, R. Babbush, *et al.*, "Quantum supremacy using a programmable superconducting processor," Nature **574**, 505–510 (2019).
2. H.-S. Zhong, H. Wang, Y.-H. Deng, *et al.*, "Quantum computational advantage using photons," Science **370**, 1460–1463 (2020).
3. T. M. Graham, Y. Song, J. Scott, *et al.*, "Multi-qubit entanglement and algorithms on a neutral-atom quantum computer," Nature **604**, 457–462 (2022).
4. S. Ebadi, T. T. Wang, H. Levine, *et al.*, "Quantum phases of matter on a 256-atom programmable quantum simulator," Nature **595**, 227–232 (2021).
5. S. Debnath, N. M. Linke, C. Figgatt, *et al.*, "Demonstration of a small programmable quantum computer with atomic qubits," Nature **536**, 63–66 (2016).
6. C. D. Bruzewicz, J. Chiaverini, R. McConnell, *et al.*, "Trapped-ion quantum computing: progress and challenges," Appl. Phys. Rev. **6**, 021314 (2019).
7. J. M. Pino, J. M. Dreiling, C. Figgatt, *et al.*, "Demonstration of the trapped-ion quantum CCD computer architecture," Nature **592**, 209–213 (2021).
8. N. H. Wan, T.-J. Lu, K. C. Chen, *et al.*, "Large-scale integration of artificial atoms in hybrid photonic circuits," Nature **583**, 226–231 (2020).
9. M. H. Abobeih, Y. Wang, J. Randall, *et al.*, "Fault-tolerant operation of a logical qubit in a diamond quantum processor," Nature **606**, 884–889 (2022).
10. A. Omran, H. Levine, A. Keesling, *et al.*, "Generation and manipulation of Schrödinger cat states in Rydberg atom arrays," Science **365**, 570–574 (2019).
11. K. Wright, K. M. Beck, S. Debnath, *et al.*, "Benchmarking an 11-qubit quantum computer," Nat. Commun. **10**, 5464 (2019).

12. A. Rahim, A. Hermans, B. Wohlfeil, *et al.*, "Taking silicon photonics modulators to a higher performance level: state-of-the-art and a review of new technologies," Adv. Photon. **3**, 024003 (2021).
13. A. Rahim, T. Spuesens, R. Baets, *et al.*, "Open-access silicon photonics: current status and emerging initiatives," Proc. IEEE **106**, 2313–2330 (2018).
14. M. Smit, K. Williams, and J. van der Tol, "Past, present, and future of InP-based photonic integration," APL Photon. **4**, 050901 (2019).
15. A. Rahim, E. Ryckeboer, A. Z. Subramanian, *et al.*, "Expanding the silicon photonics portfolio with silicon nitride photonic integrated circuits," J. Lightwave Technol. **35**, 639–649 (2017).
16. T. J. Morin, L. Chang, W. Jin, *et al.*, "CMOS-foundry-based blue and violet photonics," Optica **8**, 755–756 (2021).
17. J. F. Bauters, M. J. R. Heck, D. D. John, *et al.*, "Planar waveguides with less than 0.1 dB/m propagation loss fabricated with wafer bonding," Opt. Express **19**, 24090–24101 (2011).
18. H. El Dirani, L. Youssef, C. Petit-Etienne, *et al.*, "Ultralow-loss tightly confining Si_3N_4 waveguides and high-Q microresonators," Opt. Express **27**, 30726–30740 (2019).
19. G. Liang, H. Huang, A. Mohanty, *et al.*, "Robust, efficient, micrometre-scale phase modulators at visible wavelengths," Nat. Photonics **15**, 908–913 (2021).
20. P. R. Stanfield, A. J. Leenheer, C. P. Michael, *et al.*, "CMOS-compatible, piezo-optomechanically tunable photonics for visible wavelengths and cryogenic temperatures," Opt. Express **27**, 28588–28605 (2019).
21. H. Tian, J. Liu, B. Dong, *et al.*, "Hybrid integrated photonics using bulk acoustic resonators," Nat. Commun. **11**, 3073 (2020).
22. M. Dong, G. Clark, A. J. Leenheer, *et al.*, "High-speed programmable photonic circuits in a cryogenically compatible, visible–near-infrared 200 mm CMOS architecture," Nat. Photonics **16**, 59–65 (2022).
23. Y. H. D. Lee and M. Lipson, "Back-end deposited silicon photonics for monolithic integration on CMOS," IEEE J. Sel. Top. Quantum Electron. **19**, 8200207 (2013).
24. Z. Wang, S.-J. Chang, C.-Y. Ni, *et al.*, "A high-performance ultracompact optical interleaver based on double-ring assisted Mach–Zehnder interferometer," IEEE Photon. Technol. Lett. **19**, 1072–1074 (2007).
25. W. Bogaerts, M. Fiers, and P. Dumon, "Design challenges in silicon photonics," IEEE J. Sel. Top. Quantum Electron. **20**, 8202008 (2014).
26. I. Christen, M. Sutula, T. Propson, *et al.*, "An integrated photonic engine for programmable atomic control," arXiv, arXiv:2208.06732 (2022).
27. S. H. Tao, Q. Fang, J. F. Song, *et al.*, "Cascade wide-angle Y-junction 1 × 16 optical power splitter based on silicon wire waveguides on silicon-on-insulator," Opt. Express **16**, 21456–21461 (2008).
28. F. Van Laere, G. Roelkens, M. Ayre, *et al.*, "Compact and highly efficient grating couplers between optical fiber and nanophotonic waveguides," J. Lightwave Technol. **25**, 151–156 (2007).
29. M. A. Nielsen and I. Chuang, *Quantum Computation and Quantum Information* (2002).
30. H. Bernien, S. Schwartz, A. Keesling, *et al.*, "Probing many-body dynamics on a 51-atom quantum simulator," Nature **551**, 579–584 (2017).
31. M. Morgado and S. Whitlock, "Quantum simulation and computing with Rydberg-interacting qubits," AVS Quantum Sci. **3**, 023501 (2021).
32. H. Levine, A. Keesling, G. Semeghini, *et al.*, "Parallel implementation of high-fidelity multiqubit gates with neutral atoms," Phys. Rev. Lett. **123**, 170503 (2019).
33. R. Debroux, C. P. Michaels, C. M. Purser, *et al.*, "Quantum control of the tin-vacancy spin qubit in diamond," Phys. Rev. X **11**, 041041 (2021).
34. W. Bogaerts, P. De Heyn, T. Van Vaerenbergh, *et al.*, "Silicon microring resonators," Laser Photon. Rev. **6**, 47–73 (2012).
35. D. M. Gill, S. S. Patel, M. Rasras, *et al.*, "CMOS-compatible Si-ring-assisted Mach–Zehnder interferometer with internal bandwidth equalization," IEEE J. Sel. Top.Quantum Electron. **16**, 45–52 (2010).
36. X. L. Zhang, A. T. Gill, L. Isenhower, *et al.*, "Fidelity of a Rydberg-blockade quantum gate from simulated quantum process tomography," Phys. Rev. A **85**, 042310 (2012).
37. Y. Huang, Q. Cheng, Y.-H. Hung, *et al.*, "Multi-stage 8 × 8 silicon photonic switch based on dual-microring switching elements," J. Lightwave Technol. **38**, 194–201 (2020).
38. T. Lipka, M. Kiepsch, H. K. Trieu, *et al.*, "Hydrogenated amorphous silicon photonic device trimming by UV-irradiation," Opt. Express **22**, 12122–12132 (2014).
39. G. De Paoli, S. L. Jantzen, T. D. Bucio, *et al.*, "Laser trimming of the operating wavelength of silicon nitride racetrack resonators," Photon. Res. **8**, 677–683 (2020).
40. C. L. Panuski, I. Christen, M. Minkov, *et al.*, "A full degree-of-freedom spatiotemporal light modulator," Nat. Photonics **16**, 834–842 (2022).
41. A. Teshigahara, K.-Y. Hashimoto, and M. Akiyama, "Scandium aluminum nitride: highly piezoelectric thin film for RF SAW devices in multi GHz range," in *IEEE International Ultrasonics Symposium* (2012).
42. T. Johansson and J. Fritzin, "A review of watt-level CMOS RF power amplifiers," IEEE Trans. Microwave Theory Tech. **62**, 111–124 (2013).
43. G. N. West, W. Loh, D. Kharas, *et al.*, "Low-loss integrated photonics for the blue and ultraviolet regime," APL Photon. **4**, 026101 (2019).
44. S. Pezzagna and J. Meijer, "Quantum computer based on color centers in diamond," Appl. Phys. Rev. **8**, 011308 (2021).
45. D. A. Abanin, E. Altman, I. Bloch, *et al.*, "Colloquium: many-body localization, thermalization, and entanglement," Rev. Mod. Phys. **91**, 021001 (2019).
46. Z. Yan, Y.-C. Wang, N. Ma, *et al.*, "Topological phase transition and single/multi anyon dynamics of Z2 spin liquid," npj Quantum Mater. **6**, 1–6 (2021).